Delft University of Technology

Stable Spinning Deployment Control of a Triangle Tethered Formation System

Zhang, Fan; Zhou, He; Huang, Panfeng; Guo, Jian

Important note
To cite this publication, please use the final published version (if applicable).
Please check the document version above.

Stable Spinning Deployment Control of a Triangle Tethered Formation System

Fan Zhang, *Member, IEEE*, He Zhou, Panfeng Huang, *Senior Member, IEEE*, and Jian Guo

Abstract—The tethered formation system has been widely studied due to its extensive use in aerospace engineering, such as Earth observation, orbital location, and deep space exploration. The deployment of such a multitethered system is a problem because of the oscillations and complex formation maintenance caused by the space tether's elasticity and flexibility. In this article, a triangle tethered formation system is modeled, and an exact stable condition for the system's maintaining is carefully analyzed, which is given as the desired trajectories; then, a new control scheme is designed for its spinning deployment and stable maintenance. In the proposed scheme, a novel second-order sliding mode controller is given with a designed nonsingular sliding-variable. Based on the theoretical proof, the addressed sliding variable from the arbitrary initial condition can converge to the manifold in finite time, and then sliding to the equilibrium in finite time as well. The simulation results show that compared with classic second sliding-mode control, the proposed scheme can speed up the convergence of the states and sliding variables.

Index Terms—Stable and spinning deployment, tethered satellites system, triangle formation.

I. Introduction

EVER since Tsiolkovsky addressed a bold idea that a flexible tether is used to carry out space missions in 1895, space tether has been always considered as an extended application of the traditional rigid connected spacecraft. Tether is extendable, flexible, and can be stored in a very small size before launch. Thus, space tether has been addressed for space orbital transfer, satellite attitude stabilization, momentum transfer, etc. Based on several space experiments (TSS-1, 1992; SEDS-1, 1993), the material and the deployment/retrieval mechanism of tether in space had

Fig. 1. Schematic of the NASA-SPECS.

been practically verified, which gave great confidence to the researchers and engineers [1].

Besides the applications of single space tether, multitethers in space (as shown in Fig. 1) is another research focus of further space missions, such as artificial-gravity space station, Earth observation, deep space exploration [2], [3], etc. Compared to the traditional multisatellites formation, the connected tether between adjacent satellites provides a more precise orbital position, relative attitude, and less fuel consumption.

Thus, there have been many publications of space multi-tethered formation system. For different missions, different tethered formations have been addressed, such as the triangle formation, double-pyramid, hub-spoke formation, etc. As a classic formation of space observation, a triangle tethered formation system has been considered as a practicable structure due to its easy expandability and spatial-orientation stability in spinning case. Misra and Modi [2] and Modi *et al.* [4] had summarized early studies on dynamics and control of space tether. Kim and Hall [5] used the variable tether length to control the triangle formation. Nakaya used a PID controller based on a virtual structure dynamics to study the deployment and retrieval of the formation. Besides the theoretical study, they also built the ground experimental system with air bearing table [6]. The deployment and retrieval of the formation in an elliptic orbit is studied by Kumar and Yasaka, while it was only an open-loop controller [7]. Topal and Daybelge [8] studied the numerical solutions of a triangular formation in a circular orbit and discussed the stability of attitude motion. Flexibility of tether is considered by Williams *et al.* [9], [10]. Based on the bead model, tethers' flexibility is involved, and the optimal control scheme is utilized to solve the deployment problem. Based on the theoretical research, the practical applications of
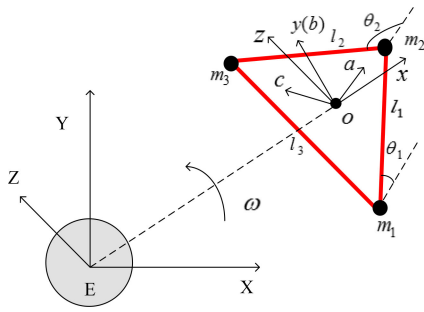
Fig. 2.   System description.

triangle formation have been addressed by NASA [11], which is called the submillimeter probe of the evolution of cosmic structure mission (SPECS), and its ground experiment of the deployment was done by MIT [12].

Although the triangle formation has been studied a lot, there are still some problems. Most of the research is based on a rigid and inelastic tether model, which has greatly reduced the difficulty of the controller design. The longitudinal oscillation due to the elasticity of the tether, along with the lateral oscillation of the space tether caused by the Coriolis force, makes the control problem complex. Williams built the motion equations based on the bead model, which can represent the flexibility of tether [9], [10]. But the model is too complex to perform real-time calculation, and which is solved by optimal control. Guang *et al.* [13] proposed a disturbance observer-based controller to exactly estimate the the disturbance during deployment. In [13], different deployment strategies of the spinning rate and tether length are studied. Qi and Misra [15] proposed open-loop charge control strategies based on the analyzed static equilibrium. Kim and Hall studied triangle tethered formation based on input-state feedback linearization in [5], but have not considered the perturbation effects. Besides the centralized control scheme, decentralised fault-tolerant control is proposed by Zhang *et al.* [16]. Based on the previous research, it is found that the connected tethers in triangle formation can be considered as a rigid elastic link during the entire deployment, because of the centripetal force caused by spinning. According to the motion characteristics of the system, the principal requirements of the formation's deployment are quickness, stability, and consistency. In consequence, the system can quickly achieve the stable spinning condition (will be discussed in Section III) and maintain in the desired formation. Besides, a tethered formation system is too complex to build a totally precise dynamics model. In this case, a controller with strong robustness is necessary for system deployment.

The sliding-mode control has been extensively applied in practical engineering due to its effective achievement, and strong robustness to the uncertainties [17], [18]. The advantages of sliding-mode control can solve the problems of the tethered formation system. But the chattering output and asymptotic stability are two weak points of sliding-mode control. To fill the gap of finite-time convergence, terminal sliding-mode control (TSMC) [19] and second-order (specifically super-twisting) sliding-mode control (STSMC) [20], [21] have been proposed. In recent years, both the TSMC and

STSMC have been continuously improved. The robustness of STSMC has been improved through adaptive gains [22], [23] and disturbance suppression [24], [25]. The sliding variable of TSMC has also been improved, and different nonlinear sliding variables are addressed [26], [27]. Each of the two controllers has its merit and demerit. STSMC can attenuate the chattering, but the finite-time convergence on the sliding manifold cannot be guaranteed. TSMC can achieve the finite-time convergence of the states to equilibrium points, but the chattering problem is not solved. To solve the above problems of tethered formation, finite-time convergence and continuous control output should be figured out simultaneously.

Therefore, in this article, an effective deployment control scheme of a tethered triangle formation system is proposed, by using a second-order sliding-mode control with a nonsingular sliding manifold, which can achieve the desired stable spinning quickly and symmetrically, and suppress the tethers' oscillation as well. Because the transition process from the initial state to the desired state is not stable, the desired spinning rate should be achieved as soon as possible. In the existing papers, it generally uses half orbits to reach a stable spinning condition. Under the proposed second-order sliding-mode controller with a nonsingular sliding variable, the stable spinning rate can be achieved within 0.2 orbits, and during the entire process of deployment, the formation is nicely symmetrical.

The remainder of this article is organized as follows. Section II introduces the dynamics modeling of the tethered triangle formation system in detail. In Section III, the derived equations of motion have been carefully analyzed, and the stable spinning conditions are derived. The proposed second-order sliding-mode controller with a nonlinear sliding variable is designed and verified in Section IV. In Section V, the proposed scheme is verified by numerical simulation, including the presentations of each state and the formation during the entire deployment process. Finally, Section V concludes with a summary of this article and a few suggestions for future research.

II. DYNAMICS MODELING

The system consists of three satellites that are connected via flexible tethers, and the entire system is a closed triangle. The exact mission scenario, including the deployment phase, stable spinning phase, and retrieval phase, has been introduced in [1]. A detailed description of the triangle formation system has been given in Fig. 2.

The assumptions used in this article are given as follows.

A1: The satellites in the formation system are treated as mass points due to their relatively small sizes compared to the connected tether's length.

A2: The flexibly connected tether has been simplified as a massless rigid noncompressed link because the tether is tight during the entire spinning deployment.

A3: The system is assumed to be on the Keplerian circular orbit, and the constant orbital velocity is Ω.

A4: The system rotates about the system centroid in an orbit plane.

Similar to the dynamics modeling in [1], the equations of motion are derived from the Lagrangian mechanics. The initial

frame $(E-XYZ)$ and orbit frame $(o-xyz)$ are defined in Fig. 2. The system energy is given as

$$T_t = \frac{1}{2} \sum_{i=1}^{3} m_i v_i^2 = \frac{1}{2} \sum_{i=1}^{3} m_i \big(\dot{\boldsymbol{R}}_0 + \dot{\boldsymbol{r}}_i\big)^2$$

$$= \frac{1}{2} m \omega^2 R_0^2 + \frac{1}{6} m \sum_{i=1}^{3} \dot{r}_i^2 \tag{1}$$

where m_i is the satellite's mass, $m = m_1 + m_2 + m_3$ is the total mass of the system, $\boldsymbol{R}_0$ denotes the position vector of the system centroid with respect to the Earth center, $\boldsymbol{r}_i (i = 1, 2, 3)$ denotes the position vector with respect to orbit frame, and ω is a constant rate of true normally angle τ.

The length of each connected tether is defined as l_i $(i = 1, 2, 3)$, and the definitions of angles θ_1 and θ_2 are given in Fig. 2. With the geometrical relationship, we can obtain

$$\begin{cases} x_2 = x_1 + l_1 \cos\theta_1 \\ y_2 = y_1 + l_1 \sin\theta_1 \\ x_3 = x_2 + l_2 \cos\theta_2 \\ y_3 = y_2 + l_2 \sin\theta_2 \end{cases} \tag{2}$$

where $(x_i \ y_i \ z_i)^T (i = 1, 2, 3)$ represents the position vector $\boldsymbol{r}_i (i = 1, 2, 3)$.

The potential energy of the system is formulated as

$$V_{t1} = -\frac{1}{3} m \sum_{i=1}^{3} \frac{\mu}{|\boldsymbol{R}_i|} = -\frac{1}{3} m \sum_{i=1}^{3} \frac{\mu}{|\boldsymbol{R}_0 + \boldsymbol{r}_i|} \tag{3}$$

where

$$1/|\boldsymbol{R}_i| = 1/|\boldsymbol{R}_0 + \boldsymbol{r}_i| = \Big(1 + 2\boldsymbol{R}_0\boldsymbol{r}_i/R_0^2 + r_i^2/R_0^2\Big)^{-\frac{1}{2}} \Big/ R_0$$

$$\approx \Big[1 - x_i/R_0 + \big(2x_i^2 - y_i^2\big)/2R_0^2\Big]/R_0. \tag{4}$$

The tension of the connected tether does not compress. According to Hooke's law of the elastic tethers, the elastic potential energy of the system can be expressed as

$$V_{t2} = \frac{1}{2} \frac{EA}{l_0} \Big[(l_1 - l_0)^2 e_1 + (l_2 - l_0)^2 e_2 + (l_3 - l_0)^2 e_3\Big] \tag{5}$$

where EA is the elastic coefficient that is decided by the tether's material; l_0 is the nature length of each tether, and parameter $e_i(i = 1, 2, 3) = \begin{cases} 1, & l_i > l_0 \\ 0, & l_i \leq l_0 \end{cases}$ is represented to the tether's real length. Based on the cosine law, l_3 in (5) can be exactly presented as $l_3 = [l_1^2 + l_2^2 + 2l_1 l_2 \cos(\theta_1 - \theta_2)]^{(1/2)}$.

The lengths of tether l_1 and l_2, angles between tethers, and coordinates θ_1 and θ_2 are defined as generalized coordinates. The equations with respect to time change with respect to orbit, and the dimensional tether length changes to the nondimensional one, which is detailedly written as

$$\begin{cases} \frac{d(\cdot)}{dt} = \frac{d(\cdot)}{d\tau} \frac{d\tau}{dt} = (\cdot)' \omega \\ l_i = \Lambda_i L_{ri} \end{cases} \tag{6}$$

where L_{ri} is reference length of tether, and $\Lambda_i \in (0, 1]$ denotes the nondimensional length of tether l_i. To further simplify the system, it is generally assumed that each mass of the satellite is the same and, similarly, the reference length of tether is the same with each other.

According to the Lagrangian mechanics $(d/dt)(\partial T/\partial \dot{q}_i) - (\partial T/\partial q_i) + (\partial V/\partial q_i) = 0$, the motion equations governing the system is derived as

$$\boldsymbol{M}(\boldsymbol{q})\boldsymbol{q}'' + \boldsymbol{C}(\boldsymbol{q}, \boldsymbol{q}')\boldsymbol{q}' + \boldsymbol{G}(\boldsymbol{q}) + \boldsymbol{P}(\boldsymbol{q}) = \boldsymbol{Q} \tag{7}$$

where $\boldsymbol{q} = [\Lambda_1 \ \Lambda_2 \ \theta_1 \ \theta_2]^T$ is the nondimensional generalized coordinate vector, and $\boldsymbol{Q} = [1/(m\omega^2 l_0)][Q_{l_1} \ Q_{l_2} \ Q_{\theta_1}/l_0 \ Q_{\theta_2}/l_0]^T$ is the corresponding generalized control force vector. The other matrices in (7) are

$$\boldsymbol{M} = \frac{1}{9} \begin{bmatrix} 2 & \tilde{\tilde{\theta}} & 0 & \Lambda_2\tilde{\theta} \\ \tilde{\tilde{\theta}} & 2 & -\Lambda_1\tilde{\theta} & 0 \\ 0 & -\Lambda_1\tilde{\theta} & 2\Lambda_1^2 & \Lambda_1\Lambda_2\tilde{\tilde{\theta}} \\ \Lambda_2\tilde{\theta} & 0 & \Lambda_1\Lambda_2\tilde{\tilde{\theta}} & 2\Lambda_2^2 \end{bmatrix}$$

$$\boldsymbol{C} = \frac{1}{9} \begin{bmatrix} 0 & \tilde{\theta}_2'\tilde{\theta} & -2\Lambda_1\tilde{\theta}_1' & -\Lambda_2\tilde{\theta}_2'\tilde{\tilde{\theta}} + \Lambda_2'\tilde{\theta} \\ -\tilde{\theta}_1'\tilde{\theta} & 0 & -\Lambda_1\tilde{\theta}_1'\tilde{\tilde{\theta}} - \Lambda_1'\tilde{\theta} & -2\Lambda_2\tilde{\theta}_2' \\ 2\Lambda_1\tilde{\theta}_1' & \Lambda_1\tilde{\theta}_2'\tilde{\tilde{\theta}} & 2\Lambda_1\Lambda_1' & \Lambda_1\Lambda_2\tilde{\theta}\tilde{\theta}_2' + \Lambda_1\Lambda_2'\tilde{\tilde{\theta}} \\ \Lambda_2\tilde{\theta}_1'\tilde{\tilde{\theta}} & 2\Lambda_2\tilde{\theta}_2' & -\Lambda_1\Lambda_2\tilde{\theta}_1'\tilde{\theta} + \Lambda_1'\Lambda_2\tilde{\tilde{\theta}} & 2\Lambda_2\Lambda_2' \end{bmatrix}$$

$$\boldsymbol{G} = \frac{1}{3} \begin{bmatrix} -(2\Lambda_1 \cos\theta_1 + \Lambda_2 \cos\theta_2) \cos\theta_1 \\ -(\Lambda_1 \cos\theta_1 + 2\Lambda_2 \cos\theta_2) \cos\theta_2 \\ \Lambda_1(2\Lambda_1 \cos\theta_1 + \Lambda_2 \cos\theta_2) \sin\theta_1 \\ \Lambda_2(\Lambda_1 \cos\theta_1 + 2\Lambda_2 \cos\theta_2) \sin\theta_2 \end{bmatrix}$$

$$\boldsymbol{P} = \frac{EA}{m\omega^2 l_0} \begin{bmatrix} (\Lambda_1 - 1)e_1 + \frac{\Lambda_3 - 1}{\Lambda_3} e_3 \big[\Lambda_1 + \Lambda_2\tilde{\tilde{\theta}}\big] \\ (\Lambda_2 - 1)e_2 + \frac{\Lambda_3 - 1}{\Lambda_3} e_3 \big[\Lambda_2 + \Lambda_1\tilde{\tilde{\theta}}\big] \\ -(\Lambda_3 - 1)e_3 \frac{\Lambda_1\Lambda_2}{\Lambda_3}\tilde{\theta} \\ (\Lambda_3 - 1)e_3 \frac{\Lambda_1\Lambda_2}{\Lambda_3}\tilde{\theta} \end{bmatrix} \tag{8}$$

where $\tilde{\theta} = \sin(\theta_1 - \theta_2)$, $\tilde{\tilde{\theta}} = \cos(\theta_1 - \theta_2)$, $\tilde{\theta}_1 = \theta_1 + 2$, and $\tilde{\theta}_2 = \theta_2 + 2$. The matrix $\boldsymbol{M}$ is a symmetric positive semidefinite matrix, which satisfies $\dot{\boldsymbol{M}} - 2\boldsymbol{C}$.

III. DYNAMICS ANALYSIS

A. Dynamics Analysis

In the stable spinning phase, although all the tethers in the formation system are constant, tethers are in different tension with different rotation angles. Consequently, real tether lengths are different. For example, tether l_1 is in the maximum tension when it rotates to the radial direction with respect to the Earth, and in the minimum tension when it rotates to the tangential direction. In this section, the dynamics in (7) and (8) are discussed to acquire the desired rotation velocity.

To simplify the dynamics equations of the system, the length rate of the tether is supposed to be 0, and the tethered formation system is in a constant angular rotation. In this case, the states are given as

$$\ddot{l}_1 = \ddot{l}_2 = 0, \dot{l}_1 = \dot{l}_2 = 0$$
$$\ddot{\theta}_1 = \ddot{\theta}_2 = 0, \dot{\theta}_1 = \dot{\theta}_2 = \dot{\theta}. \tag{9}$$

As previously mentioned, the tether tension in radial ($\theta_1 = 0$(rad)) and tangential [$\theta_1 = (\pi/2)$(rad)] direction can reach the extremum value. Accordingly, the elastic deformation ε_i

of tether is derived as

$$\begin{cases} \varepsilon_1|_{\theta_1=0} = l_0\left[\left(\frac{\dot{\theta}}{\omega}+1\right)^2 + \frac{7}{2}\right] \Big/ \left\{\frac{9EA}{m\omega^2 l_0} - \left[\left(\frac{\dot{\theta}}{\omega}+1\right)^2 + \frac{7}{2}\right]\right\} \\ \varepsilon_2|_{\theta_1=0} = \varepsilon_3|_{\theta_1=0} \\ \quad = l_0\left[\left(\frac{\dot{\theta}}{\omega}+1\right)^2 - 1\right] \Big/ \left\{\frac{9EA}{m\omega^2 l_0} - \left[\left(\frac{\dot{\theta}}{\omega}+1\right)^2 - 1\right]\right\} \\ \varepsilon_1|_{\theta_1=\frac{\pi}{2}} = l_0\left[\left(\frac{\dot{\theta}}{\omega}+1\right)^2 - \frac{5}{2}\right] \Big/ \left\{\frac{9EA}{m\omega^2 l_0} - \left[\left(\frac{\dot{\theta}}{\omega}+1\right)^2 - \frac{5}{2}\right]\right\} \\ \varepsilon_2|_{\theta_1=\frac{\pi}{2}} = \varepsilon_3|_{\theta_1=\frac{\pi}{2}} \\ \quad = \left\{l_0\left[\left(\frac{\dot{\theta}}{\omega}+1\right)^2 + 2\right] \Big/ \frac{9EA}{m\omega^2 l_0} - \left[\left(\frac{\dot{\theta}}{\omega}+1\right)^2 + 2\right]\right\}. \end{cases}$$
(10)

According to the extremum values of the tether's elastic deformations, (10) can be further reformulated as

$$\frac{l_0\left[\left(\frac{\dot{\theta}}{\omega}+1\right)^2 - \frac{5}{2}\right]}{\frac{9EA}{m\omega^2 l_0} - \left[\left(\frac{\dot{\theta}}{\omega}+1\right)^2 - \frac{5}{2}\right]} \leq \varepsilon \leq \frac{l_0\left[\left(\frac{\dot{\theta}}{\omega}+1\right)^2 + \frac{7}{2}\right]}{\frac{9EA}{m\omega^2 l_0} - \left[\left(\frac{\dot{\theta}}{\omega}+1\right)^2 + \frac{7}{2}\right]}.$$
(11)

Due to the centripetal force caused by the rotation, all the tethers in the tethered formation system are in the tension, namely, $\varepsilon > 0$. Because $[(9EA)/(m\omega^2 l_0)] \gg [([\dot{\theta}/\omega] + 1)^2 - (5/2)]$, an exact nondimensional condition of the rotation velocity is derived

$$\theta' > \left(\sqrt{\frac{5}{2}} - 1\right) \text{ or } \theta' < -\left(\sqrt{\frac{5}{2}} + 1\right).$$
(12)

Remark 1: The negative sign in (12) represents the opposite rotation direction of the Earth. Therefore, if the rotation direction of the tethered formation system is in accordance with the Earth, the system's rotation angular velocity should be larger than $\sqrt{5/2} - 1$ times of the orbital angular velocity. Inversely, if the rotation direction is opposite of the Earth's rotation, the scalar of the system's rotation angular velocity should be larger than $\sqrt{5/2} + 1$ times the orbital angular velocity.

B. Simulations

To verify the results in (12), numerical simulation is given with the system dynamics in (7) and (8). The generalized control force $\boldsymbol{Q}$ is $\boldsymbol{0}$, and the initial condition $(\Lambda_1 \ \Lambda_2 \ \Lambda_1' \ \Lambda_2' \ \Lambda_1'' \ \Lambda_2'' \ \theta_1 \ \theta_2 \ \theta_1' \ \theta_2' \ \theta_1'' \ \theta_2'')^T|_0$ is $(1 \ 1 \ 0 \ 0 \ 0 \ 0 \ \pi/6 \ 5\pi/6 \ \theta' \ \theta' \ 0 \ 0)^T$, where the rotation velocity θ' is given different values to verify the results derived in (12). The other system parameters are given in Table I.

The simulation results of the system's rotation with different rotation velocities $\theta' = 0.5$ and $\theta' = 1$ are given in Figs. 3 and 4, respectively. According to the result in (12), it is known that $\theta' = 0.5$ does not satisfy the stable rotation condition, while $\theta' = 1$ satisfies. The direction of the system's rotation is according to the Earth's rotation. It is obvious that the system formation of $\theta' = 1$ is stable during the rotation, while the case $\theta' = 0.5$ is unstable. Each tether in the formation can be kept in tiny tension during the rotation when $\theta' = 1$, and the rotation velocity can be stably kept in the initial condition
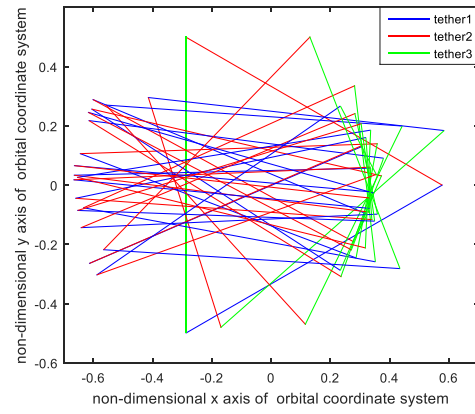

Fig. 3. System formation when $\theta' = 0.5$.
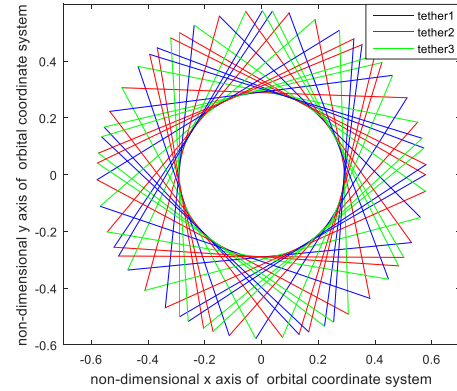
Fig. 4. System formation when $\theta' = 1$.

TABLE I
SYSTEM PARAMETERS

Parameters	Values
total mall of the satellites m/kg	3600
elasticity modulus MPa	300000
natural length of the tether l_0/m	1000
orbital velocity $\omega/(\text{rad/s})$	0.00007

without any generalized control force. All the results verify that the conditions of stable rotation given in (12) are correct, and the results will be used in the controller design of the system's deployment.

Besides, two given certain values of rotation velocity, the relationship between the rotation velocity and elastic deformation has also been given in Fig. 5. According to the analytic conclusions given in (12), the rotation velocity in region $\theta' \in [-\sqrt{5/2} - 1, \sqrt{5/2} - 1]$ will result in unstable formation. In the dash-line box of Fig. 5, both ε_2 and ε_3 are not positive, which mean tethers l_2 and l_3 are slack. The slack tethers cannot maintain a stable rotating formation. The simulation results agree to the analytic conclusions in (12).

IV. CONTROL SCHEME DESIGN

Based on the dynamics analysis, a set of desired rotation velocity is acquired for the deployment controller design. From the previous knowledge of the single tether's deployment [25],

Fig. 5. Relationship between θ' and ε.

it is known that the deployment/retrieval of the tether in space will cause oscillations due to the orbital Coriolis forces. For this proposed triangle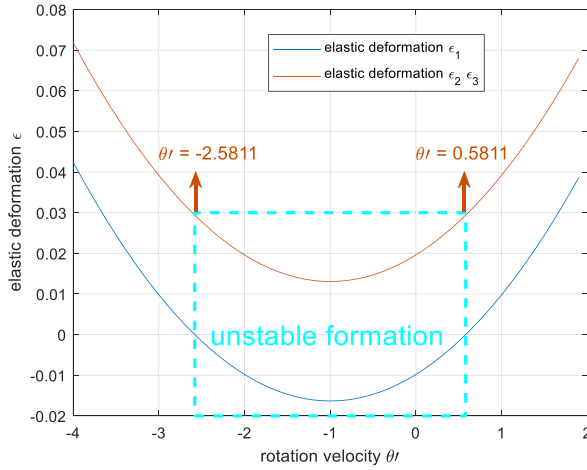 tethered formation system, the unstable spinning rotation during the deployment complicates the problem. To suppress the disturbance caused by oscillation and deploy the desired spinning rate exactly and quickly, a new control scheme is proposed, which can enforce the generalized coordinates to converge to the desired states under the desired strategy in finite time. A new second-order sliding-mode control with a nonsingular sliding manifold is designed in this section.

A. Problem Formulation

For controller design and concise expression, the dynamics equations in (7) and (8) are reformulated by considering the space environment perturbation as

$$\begin{cases} x'_{i1} = x_{i2} \\ x'_{i2} = f_i(\boldsymbol{x}) + g_i(\boldsymbol{x})u_i + d_i \end{cases} \tag{13}$$

where functions $f_i(\boldsymbol{x})$ and $g_i(\boldsymbol{x})u_i$ are, respectively, derived equal to $\{-\boldsymbol{M}^{-1}[\boldsymbol{C}(\boldsymbol{q}, \boldsymbol{q}')\boldsymbol{q}' + \boldsymbol{G}(\boldsymbol{q}) + \boldsymbol{P}(\boldsymbol{q})]\}_i$ and $[\boldsymbol{M}^{-1}\boldsymbol{Q}]_i$ with $i = \Lambda_1, \Lambda_2, \theta_1, \theta_2$, which corresponds to the generalized coordinates $\boldsymbol{q} = [\Lambda_1 \ \Lambda_2 \ \theta_1 \ \theta_2]^T$ given in (7). The system state vector is a smooth nonlinear function, $u_i \in \mathbb{R}$ denotes the control input, and $d_i \in \mathbb{R}$ is the uncertainty due to orbital perturbation, such as aerodynamic drag, solar radiation pressure, and the oscillation of the connected tether.

Because of the simplifications used in Section II, system dynamics $f_i(\boldsymbol{x})$ should be further formulated as

$$f_i(\boldsymbol{x}) := \bar{f}_i(\boldsymbol{x}) + \Delta f_i(\boldsymbol{x}) \tag{14}$$

where $\bar{f}_i(\boldsymbol{x})$ denotes the nominal function and $\Delta f_i(\boldsymbol{x})$ denotes the dynamics uncertainties that are bounded.

B. Preliminary

Based on [25] and [26], a nonlinear sliding variable $\sigma_i(\boldsymbol{x}_i, t)$ for each generalized coordinate is designed as

$$\sigma_i(\boldsymbol{x}_i, t) := x_{i2} + \int \left[\kappa_1 |x_{i1}|^{\lambda_1 - 1} x_{i1} + \kappa_2 |x_{i2}|^{\lambda_2 - 1} x_{i2} \right] \mathrm{d}\tau \tag{15}$$

where κ_i is a positive constant and λ_i satisfies $0 < \lambda_i < 1$ with $i = 1, 2$. The derivative of $\sigma_i(\boldsymbol{x}_i, t)$ with respect to the orbit is given as

$$\sigma'_i(\boldsymbol{x}_i, t) = x'_{i2} + \kappa_1 |x_{i1}|^{\lambda_1 - 1} x_{i1} + \kappa_2 |x_{i2}|^{\lambda_2 - 1} x_{i2}. \tag{16}$$

According to (13) and (14), (16) can be expressed as

$$\sigma'_i(\boldsymbol{x}_i, t) = \bar{f}_i(\boldsymbol{x}) + g_i(\boldsymbol{x})u_i + \kappa_1 |x_{i1}|^{\lambda_1 - 1} x_{i1} + \kappa_2 |x_{i2}|^{\lambda_2 - 1} x_{i2} \\ \underbrace{+ \Delta f_i(\boldsymbol{x}) + d_i}_{\phi_i(\boldsymbol{x}_i, t)} \tag{17}$$

where $\phi_i(\boldsymbol{x}_i, t) = \Delta f_i(\boldsymbol{x}) + d_i$ denotes the uncertainties [21].

Assumption 1: The given uncertainties $\phi_i(\boldsymbol{x}_i, t) \in \mathbb{R}$ should satisfy $|\phi_i(\boldsymbol{x}_i, t)| \leq \tilde{\delta}_{i1}(|\sigma_i(\boldsymbol{x}_i, t)|)$, where δ_{i1} is continuous and will be designed later [24].

Remark 2: Due to the definition of the states in (7), it can be obtained that $x_i \in \mathcal{L}_\infty$ and $\|\boldsymbol{x}_i\|_\infty = \sup |\boldsymbol{x}_i| < \infty$. The main disturbance of a tethered formation system is the oscillations of connected tethers between the satellites, and orbital perturbations. By the comparison, tether oscillations that are caused by the Coriolis force play a major role. It is studied that tether's oscillation is damped amplitude oscillations [25]. Therefore, $\phi_i(\boldsymbol{x}_i, t)$ in the proposed application is boundary and unknown.

Remark 3: The upper bound $\tilde{\delta}_{i1} \in \mathbb{R}^+$ is the maximum of δ_{i1}. Because $\delta_{i1}(|\sigma_i(\boldsymbol{x}_i, t)|)$ is defined as a function of the sliding variable, it vanishes as the sliding manifold $\sigma_i(\boldsymbol{x}_i, t) = 0$ is approached.

C. Controller Development and Stability Analysis

Design the control input u_i as

$$\begin{cases} u_i = g_i^{-1} \left[-\bar{f}_i - \kappa_1 |x_{i1}|^{\lambda_1 - 1} x_{i1} - \kappa_2 |x_{i2}|^{\lambda_2 - 1} x_{i2} + v \right] \\ v_i = -\mu_{i1} \delta_{i1}(\sigma_i) + w_i + \phi_i(\boldsymbol{x}_i, t) \\ w'_i = -\mu_{i2} \delta_{i2}(\sigma_i) \\ \delta_{i1} := \eta_i(|\sigma_i|) sgn(\sigma_i) \\ \delta_{i2} := \eta_i(|\sigma_i|) \eta'_i(|\sigma_i|) sgn(\sigma_i) \end{cases} \tag{18}$$

where η_i is a nonlinear function of the absolute sliding variable, and η'_i is its derivative with respect to orbit, and $\mu_{i1} > 0$ and $\mu_{i2} > 0$ denotes the constant gains of the controller.

Based on (16)–(18), the closed system dynamics with respect to the sliding variable can be derived as

$$\sigma'_i(\boldsymbol{x}_i, t) = -\mu_{i1} \delta_{i1}(\sigma_i) + \int -\mu_{i2} \delta_{i2}(\sigma_i) \mathrm{d}\tau + \phi_i(\boldsymbol{x}_i, t). \tag{19}$$

To guarantee a finite-time convergence of the proposed closed system (19), an absolutely continuous positive-definite Lyapunov function $V_i[\sigma_i(\delta_{i1}, \delta_{i2})]$ should be found. The function should be the solution of the following partial differential inequality:

$$\langle \nabla_{\delta_{i1}} V_{\delta_{i1}}, \delta_{i1} \rangle + \langle \nabla_{\delta_{i2}} V_{\delta_{i2}}, \delta_{i2} \rangle \leq -p V_i^q \tag{20}$$

where ∇ denotes the partial derivative, $\langle \cdot, \cdot \rangle$ denotes the scalar product with respect to an Euclidian space, and both p and q are certain positive constants. According to the Lyapunov stability, it is evident that the closed-loop system (19) can converge within finite time $t_{\text{reach}} \leq V_i^{1-p}[\sigma_i(0)]/q(1-p)$ in the case $p < 1$; while in the

case $p \geq 1$, (19) can only achieve an asymptotic convergence.

Theorem 1: Assume that Assumption 1 is globally satisfied. With the definition of a symmetric positive-definite matrix [which is composed by the controller gains in (18)] $\boldsymbol{P} := \begin{pmatrix} \mu_{i1}^2 + 2\mu_{i2} - \mu_{i1} & -(\mu_{i1} - 1) \\ -(\mu_{i1} - 1) & 2 \end{pmatrix}$ and the initial condition $\sigma_i'(x_{i1}|_{t=0}, x_{i2}|_{t=0})$, the sliding manifold $\sigma_i(\boldsymbol{x}_i) = 0$ can be reached in finite time $t_r \leq [(\sqrt{\lambda_{\min}(\boldsymbol{P})}\lambda_{\max}(\boldsymbol{P}))/(\min\{\lambda_{\min}(\boldsymbol{Q}_i)\})]V_i^{(1/2)}(0)$ (will be defined below) under the variable controller (18) with the gains $\mu_{i1} > 1$ and $\mu_{i2} > [(\mu_{i1} + 1)/(2(\mu_{i1} - 1))]^2 + 1$. The terms δ_{i1} and δ_{i2} in (18) are given as

$$\begin{cases} \delta_{i1}(\sigma_i) = \left[\rho_{i1}|\sigma_i|^{\frac{1}{2}} + \rho_{i2}|\sigma_i|\right]\text{sgn}(\sigma_i) \\ \delta_{i2}(\sigma_i) = \left[\frac{1}{2}\rho_{i1}^2 + \frac{3}{2}\rho_{i1}\rho_{i2}|\sigma_i|^{\frac{1}{2}} + \rho_{i2}^2|\sigma_i|\right]\text{sgn}(\sigma_i) \end{cases}. \quad (21)$$

Proof: Consider a transferred vector $\boldsymbol{\zeta}_i$ composed by the nonlinear terms δ_{i1} and δ_{i2}, which is expressed as

$$\boldsymbol{\zeta}_i = \begin{pmatrix} \zeta_{i1} \\ \zeta_{i2} \end{pmatrix} = \begin{pmatrix} \eta_i(|\sigma_i|)\text{sgn}(\sigma_i) \\ \int \eta_i(|\sigma_i|)\eta_i'(|\sigma_i|)\text{sgn}(\sigma_i)d\tau \end{pmatrix}. \quad (22)$$

The derivative of $\boldsymbol{\zeta}_i$ with respect to time is derived as

$$\boldsymbol{\zeta}_i' = \begin{pmatrix} \zeta_{i1}' \\ \zeta_{i2}' \end{pmatrix} = \eta_i'(|\sigma_i|)\boldsymbol{A}_i[\vartheta_i(\eta_i, t)]\boldsymbol{\zeta}_i \quad (23)$$

where $\boldsymbol{A}_i[\vartheta_i(\eta_i, t)] = \begin{bmatrix} -\mu_{i1} + \vartheta_i(\eta_i, t) & 1 \\ -\mu_{i2} & 0 \end{bmatrix}$ with $\vartheta_i(\eta_i, t) = [(\phi_i(\boldsymbol{x}_i, t))/(\eta_i(|\sigma_i|))]\text{sgn}(\sigma_i)$. According to Assumption 1, it is clear that $|\vartheta_i(\eta_i, t)| \leq 1$.

The determinant of $\boldsymbol{P}$ is $\det(\boldsymbol{P}) = \mu_{i1}^2 + 4\mu_{i2} - 1$. Based on the condition $\mu_{i2} > [(\mu_{i1} + 1)/(2(\mu_{i1} - 1))]^2 + 1$, it is proved that $\boldsymbol{P}$ is absolutely positive definite. With the derivative of a positive definite $\boldsymbol{P}$ and the condition $\mu_{i2} > [(\mu_{i1} + 1)/(2(\mu_{i1} - 1))]^2 + 1$, it can be obtained that $\mu_{i2} > 1/4$.

The Lyapunov candidate function [21] is selected as

$$V_i := \left(\mu_{i1}^2 + 2\mu_{i2} - \mu_{i1}\right)\|\eta_i\|_2^2 - 2(\mu_{i1} - 1)\eta_i(|\sigma_i|)\text{sgn}(\sigma_i)w_i + 2\|w_i\|_2^2 \quad (24)$$

where $\|\ \|_2$ denotes the Euclidean norm.

According to the definition of the designed transferred vector $\boldsymbol{\zeta}_i$ in (22), (24) can be reformulated as

$$V_i := \boldsymbol{\zeta}_i^T \boldsymbol{P} \boldsymbol{\zeta}_i. \quad (25)$$

Then, we have $\lambda_{\min}(\boldsymbol{P})\|\boldsymbol{\zeta}_i\|_2^2 \leq V_i = \boldsymbol{\zeta}_i^T \boldsymbol{P} \boldsymbol{\zeta}_i \leq \lambda_{\max}(\boldsymbol{P})\|\boldsymbol{\zeta}_i\|_2^2$. Due to the derivative of $\boldsymbol{\zeta}_i$ in (23), the derivative of V_i with respect to the orbit is

$$V_i' := \eta_i'(|\sigma_i|)\boldsymbol{\zeta}_i^T\left(\boldsymbol{A}_i^T\boldsymbol{P} + \boldsymbol{P}\boldsymbol{A}_i\right)\boldsymbol{\zeta}_i. \quad (26)$$

With the definition $\boldsymbol{Q}_i := -(\boldsymbol{A}_i^T\boldsymbol{P} + \boldsymbol{P}\boldsymbol{A}_i)$, (26) is

$$V_i' = -\eta_i'(|\sigma_i|)\boldsymbol{\zeta}_i^T\boldsymbol{Q}_i\boldsymbol{\zeta}_i. \quad (27)$$

Define $\bar{\lambda}_i := \min\{\lambda_{\min}(\boldsymbol{Q}_i)\}$. If $\bar{\lambda}_i$ is positive, the sliding variable can converge to the manifold asymptotically. Using the definition of $\boldsymbol{\zeta}_i$, we obtain $\|\boldsymbol{\zeta}_i\|_2^2$. But for finite-time convergence in (20), some more conditions should be satisfied. Comparing (20) and (27), it can be known that

$$V_i' \leq -\eta_i'(|\sigma_i|)\lambda_{\min}(\boldsymbol{Q}_i)\|\boldsymbol{\zeta}_i\|_2^2$$

$$\leq -\eta_i'(|\sigma_i|)\bar{\lambda}_i\|\boldsymbol{\zeta}_i\|_2^2$$

$$\leq -\eta_i'(|\sigma_i|)\frac{\bar{\lambda}_i}{\lambda_{\max}(\boldsymbol{P})}V_i. \quad (28)$$

The assumption $\bar{\lambda}_i > 0$ can be equivalent to $\boldsymbol{Q}_i > 0$. But the assumption $\min\{\lambda_{\min}(\boldsymbol{Q}_i)\} > 0$ does not always stand up, which depends on its expression. Define $p_1 := \mu_{i1}^2 + 2\mu_{i2} - \mu_{i1}$ and $p_2 := (\mu_{i1} - 1)$. Based on the definition of $\boldsymbol{A}_i[\vartheta_i(\eta_i, t)] := \begin{bmatrix} a_{i1} & 1 \\ a_{i2} & 0 \end{bmatrix}$ and symmetric positive-definite matrix $\boldsymbol{P} := \begin{bmatrix} p_1 & -p_2 \\ -p_2 & 2 \end{bmatrix}$, the exact expression of $\boldsymbol{Q}_i$ is given as

$$\boldsymbol{Q}_i = \begin{bmatrix} -2p_1a_{i1} + 2p_2a_{i2} & \bigstar \\ -p_1 + p_2a_{i1} - 2a_{i2} & 2p_2 \end{bmatrix}. \quad (29)$$

In order to satisfy $\bar{\lambda}_i > 0$, matrix $\boldsymbol{Q}_i$ is discussed. With the definition of $\boldsymbol{A}_i[\vartheta_i(\eta_i, t)]$ and the conditions $|\vartheta_i(\eta_i, t)| \leq 1$ and $\mu_{i1} > 1$, it can be known that $a_{i1} \in [-\mu_{i1} - 1, -\mu_{i1} + 1] \subset (-\infty, 0)$. Analogously, we can obtain $a_{i2} = -\mu_{i2} \subset (-\infty, -1/4)$. Accordingly, a_{i1} and a_{i2} can only be negative values, and (29) can be derived as

$$\boldsymbol{Q}_i = \begin{bmatrix} 2p_1|a_{i1}| - 2p_2|a_{i2}| & \bigstar \\ -p_1 - p_2|a_{i1}| + 2|a_{i2}| & 2p_2 \end{bmatrix} \quad (30)$$

where $|a_{i1}| \subset [\min\{|\mu_{i1} + 1|, |\mu_{i1} - 1|\}, \infty)$ and $|a_{i2}| = \mu_{i2}$.

Similarly, it is known that the bottom-right term $2p_2$ in matrix $\boldsymbol{Q}_i$ is positive due to $\mu_{i1} > 1$. For a necessary condition $\det(\boldsymbol{Q}_i) > 0$, it is acquired from (29) that

$$\det(\boldsymbol{Q}_i) = -p_1^2 + \Xi_1 p_1 - \Xi_0 \quad (31)$$

where

$$\begin{cases} \Xi_1 = 2|a_{i1}|(\mu_{i1} - 1) + 4|a_{i2}| \\ \Xi_0 = 4|a_{i2}|(\mu_{i1} - 1)^2 + [|a_{i1}|(\mu_{i1} - 1) - 2|a_{i2}|]^2 \end{cases}. \quad (32)$$

Because of the condition $\mu_{i1} > 1$, $a_{i1} \subset (-\infty, 0)$, and $a_{i2} \subset (-\infty, -1/4)$, it can be concluded that $\Xi_1 \subset (0, \infty)$ and $\Xi_2 \subset (0, \infty)$. Similarly, according to the François Viète theorem [24], the discriminant of $\det(\boldsymbol{Q}_i)$ is given as

$$\Delta = \Xi_1^2 - 4\Xi_0$$
$$= 16|a_{i2}|(\mu_{i1} - 1)[2|a_{i1}| - (\mu_{i1} - 1)]. \quad (33)$$

With the derivative $a_{i1} \in [-\mu_{i1} - 1, -\mu_{i1} + 1]$, it is known $a_{i1} \in [-\mu_{i1} - 1, -\mu_{i1} + 1]$, and $\Delta > 0$. Thus, the roots of $\det(\boldsymbol{Q}_i)$ with respect to p_1 are always real, which are expressed as

$$r_{p1\_1} = \frac{1}{2}\left(\Xi_1 - \sqrt{\Xi_1^2 - 4\Xi_0}\right)$$
$$r_{p1\_2} = \frac{1}{2}\left(\Xi_1 + \sqrt{\Xi_1^2 - 4\Xi_0}\right). \quad (34)$$

With the expression of Ξ_1 and Ξ_0 in (32), the roots r_{p1_1} and r_{p1_2} can be further expressed as

$$r_{p1\_1} = \frac{1}{2}\left\{ \begin{array}{l} 2|a_{i1}|(\mu_{i1} - 1) + 4|a_{i2}| \\ -4\sqrt{|a_{i2}|(\mu_{i1} - 1)[2|a_{i1}| - (\mu_{i1} - 1)]} \end{array} \right\}$$
$$r_{p1\_2} = \frac{1}{2}\left\{ \begin{array}{l} 2|a_{i1}|(\mu_{i1} - 1) + 4|a_{i2}| \\ +4\sqrt{|a_{i2}|(\mu_{i1} - 1)[2|a_{i1}| - (\mu_{i1} - 1)]} \end{array} \right\}. \quad (35)$$

According to the expression of $A_i[\vartheta_i(\eta_i, t)]$ and the analysis of $|a_{i1}|$ and $|a_{i2}|$, it is known that root r_{p1_2} can increase with $|a_{i1}|$ and $|a_{i2}|$. In other words, root r_{p1_2} can obtain the lower limit with the minimum $|a_{i1}|$ and $|a_{i2}|$. The lower limit of root r_{p1_2} is defined as $\underline{r}_{p1} := \min\{r_{p1\_2}\}$, which can be acquired as

$$
\begin{aligned}
\underline{r}_{p1} &= (\mu_{i1} - 1)^2 + 2\mu_{i2} + 2(\mu_{i1} - 1)\sqrt{\mu_{i2}} \\
&> (\mu_{i1} - 1)^2 + 2\mu_{i2} + (\mu_{i1} - 1) \\
&= \mu_{i1}^2 + 2\mu_{i2} - \mu_{i1}.
\end{aligned} \tag{36}
$$

Similarly, we can obtain

$$
\begin{aligned}
r_{p1\_2} &< (\mu_{i1} + 1)(\mu_{i1} - 1) + 2\mu_{i2} - (\mu_{i1} - 1) + 2 \\
&< \mu_{i1}^2 + 2\mu_{i2} - \mu_{i1}.
\end{aligned} \tag{37}
$$

It can be concluded that $r_{p1\_1} < p_1 < r_{p1\_2}$. Thus, $\bar{\lambda}$ is positive, and $\det(\boldsymbol{Q}_i)$ in (31) can be proved to be positive as well. It is proved that the inequality in (28)$V_i' \le -\eta_i'(|\sigma_i|)[\bar{\lambda}_i/(\lambda_{\max}(\boldsymbol{P}))]V_i$ makes sense. With the definition of η_i and $\boldsymbol{\zeta}_i$, we obtain

$$
\eta_i - \eta_i'|\sigma_i| = \frac{1}{2}\rho_{i1}|\sigma_i|^{\frac{1}{2}} \tag{38}
$$

and

$$
|\zeta_{i1}| - 2\eta_i'|\sigma_i| = -\rho_{i2}|\sigma_i|. \tag{39}
$$

Comparing the above two equations, the relations between η_i' and $|\zeta_{i1}|$ can be derived as $[|\zeta_{i1}|/(2|\sigma_i|)] < \eta_i' < [|\zeta_{i1}|/|\sigma_i|]$. Due to $|\zeta_{i1}| < \|\boldsymbol{\zeta}_i\|_2$ and $\lambda_{\min}(\boldsymbol{P})\|\boldsymbol{\zeta}_i\|_2^2 \le V_i = \boldsymbol{\zeta}_i^T\boldsymbol{P}\boldsymbol{\zeta}_i \le \lambda_{\max}(\boldsymbol{P})\|\boldsymbol{\zeta}_i\|_2^2$, we obtain $\eta_i' > [1/(\sqrt{\lambda_{\min}(\boldsymbol{P})})]V_i^{(1/2)}$. Thus, (28) can be further formulated as

$$
V_i' \le -\frac{\min\{\lambda_{\min}(\boldsymbol{Q}_i)\}}{\sqrt{\lambda_{\min}(\boldsymbol{P})}\lambda_{\max}(\boldsymbol{P})}V_i^{\frac{1}{2}}. \tag{40}
$$

Define $p := [(\min\{\lambda_{\min}(\boldsymbol{Q}_i)\})/(\sqrt{\lambda_{\min}(\boldsymbol{P})}\lambda_{\max}(\boldsymbol{P}))]$ and $q := (1/2)$, (39) is $V_i' \le -pV_i^q$ with are certain positive constants p and q. Then, the condition of finite-time convergence given in (20) is satisfied. To acquire the limit time of convergence, integrate both sides of this equation (39), it is

$$
t_r \le 2\frac{\sqrt{\lambda_{\min}(\boldsymbol{P})}\lambda_{\max}(\boldsymbol{P})}{\min\{\lambda_{\min}(\boldsymbol{Q}_i)\}}V_i^{\frac{1}{2}}(0). \tag{41}
$$

It is clearly proved that the designed sliding variable σ_i can reach the sliding manifold $\sigma_i \to 0$ within finite time (40) $t \to t_r$ with any initial values $\sigma_i(0)$ [28]. ∎

Remark 4: According to (18) and (19), it is known that $\sigma_i(\boldsymbol{x}_i, t)$ and w_i are absolutely continuous with respect to nondimensional time (NT) due to the differential equation (19). Thus, the Lyapunov function $V_i \in \mathbb{R}_{\ge 0}$ is also continuous due to the continuous variable $\sigma_i(\boldsymbol{x}_i, t)$ and w_i.

Remark 5: Based on (40), we obtain $V_i[\sigma_i(t)] = V_i[\sigma_i(0)] + \int_0^{t_r} V_i'd\tau < V_i[\sigma_i(0)]$ for all $t > 0$. Because of the monotone decreasing, $V_i = 0$ when $t > t_r$, and the finite-time convergence is established. From (41), it is obvious that the theoretical reaching time of the convergence depends on the initial conditions $\sigma_i(\boldsymbol{x}_i, t)|_{t=0}$. Normally, a large initial state error leads to a longer convergence time. Compared with a linear sliding variable, a nonlinear sliding variable designed in (16) can speed up the convergence time in the reaching phase.

Remark 6: There are some constant gains in the proposed control scheme and corresponding sliding variable scheme. It has been noted that the subscript i denotes different generalized coordinate. The coordinates Λ_1 and Λ_2 are relevant, and θ_1 and θ_2 are relevant. In order to maintain a desired closed triangle, each set of gain of Λ_1 and Λ_2 should be the same, and similarly θ_1 and θ_2. For example, $\eta_{\Lambda_1} = \eta_{\Lambda_2}$ should be selected in the application.

Remark 7: For practical engineering, the states in (15) can be replaced by the state errors $\varepsilon_{i1} = x_{i1} - x_{i1\_d}$ and $\varepsilon_{i2} = x_{i2} - x_{i2\_d}$, where x_{ij_d} $(j = 1, 2)$ is the desired state value. After the transformation, the control objective is changed from equilibrium states to the trajectory tracking $\varepsilon_{ij} \to 0$ $(j = 1, 2)$.

Remark 8: Equation (41) provides a finite reaching time of the closed dynamics system (19), specifically from $\sigma_i(0)$ to $\sigma_i = 0$. But after the reaching of sliding manifold, it still takes time to slide to the desired equilibrium state $(\varepsilon_{i1} \to 0$ and $\varepsilon_{i2} \to 0)$. With the proposed sliding variable in (15), the sliding dynamics on the manifold $(\varepsilon_{i1} \to 0)$ is reduced to be $\varepsilon_{i2}' = -\kappa_2|\varepsilon_{i2}|^{\lambda_2 - 1}\varepsilon_{i2}$. Thus, on the sliding manifold, ε_{i2} can converge to 0 within a finite time $t_c \le [(\kappa_2^{-\lambda_2})/(1 - \lambda_2)]|\varepsilon_{i2}(t_r)|^{1-\lambda_2}$. The total time from the initial condition $\sigma_i(0)$ to the equilibrium states $\varepsilon_{i1} \to 0$ and $\varepsilon_{i2} \to 0$ is $t := t_r + t_c$, which is certainly finite.

V. SIMULATIONS

A. Initial Conditions

As described earlier, the formation system is launched in a compact formation. The system needs to deploy to a desired formation, and then can carry out the task, such as Earth observation. The deployment of a triangle tethered formation system is numerically simulated in this section. In practical engineering, all the states are acquired by tether's releasing/retrieval mechanism and satellite's sensors. The basic information of the system parameters has been given in Table I. The initial conditions of the system are given as $\Lambda_{10} = \Lambda_{20} = 0.005$, $\Lambda_{10}' = \Lambda_{20}' = 0$, $\Lambda_{10}'' = \Lambda_{20}'' = 0$, $\theta_{10} = \pi/6.5$, $\theta_{20} = 5\pi/6.5$, $\theta_{10}' = \theta_{20}' = 0.1$, and $\theta_{10}'' = \theta_{20}'' = 0$. This initial formation means that the triangular system is in a compact rotation with low speed. According to the conclusion in Section III, an appropriate rotation speed is the key for system's maintaining. Thus, the desired states are given as $\boldsymbol{q_d} = [1 \quad 1 \quad \theta_{1d} \quad \theta_{2d}]^T$ with $\theta_{1d} = \tau\theta_{1d}'$ and $\theta_{2d} = \tau\theta_{2d}'$, $\boldsymbol{q_d'} = [0 \quad 0 \quad 3 \quad 3]^T$ and $\boldsymbol{q_d''} = [0 \quad 0 \quad 0 \quad 0]^T$.

The gains in the proposed control scheme and sliding variable scheme are given. As discussed in Remark 5, in order to keep the formation stable, the gains for Λ_1 and Λ_2 (or θ_1 and θ_2) should be the same. Thus, the gains are, $\mu_1 = $ diag[3, 3, 20, 20], $\mu_2 = $ diag[60, 60, 60, 60], $\lambda_1 = \lambda_2 = 0.5$, $\rho_1 = $ diag[1, 1, 1, 1], and $\rho_2 = $ diag[10, 10, 10, 10]. To modify the unknown and bounded disturbances in Assumption 1 and Remark 2, a sinusoidal function is used for simulation, specifically the tether oscillations caused by the Coriolis force.

B. Simulation Results

To show the effectiveness of the proposed schemes, a classic super-twisting sliding-mode control (STSMC) and an
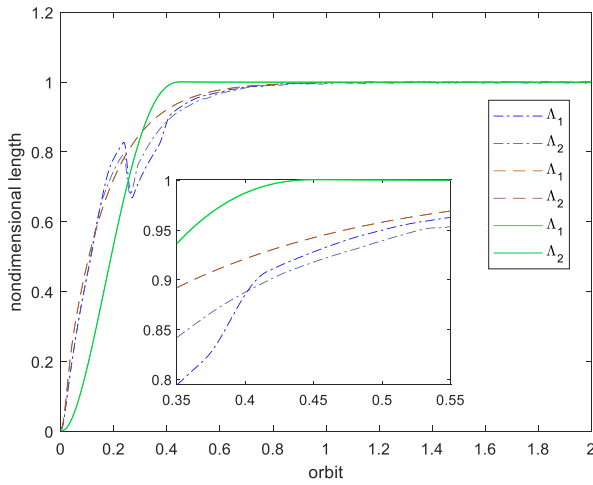
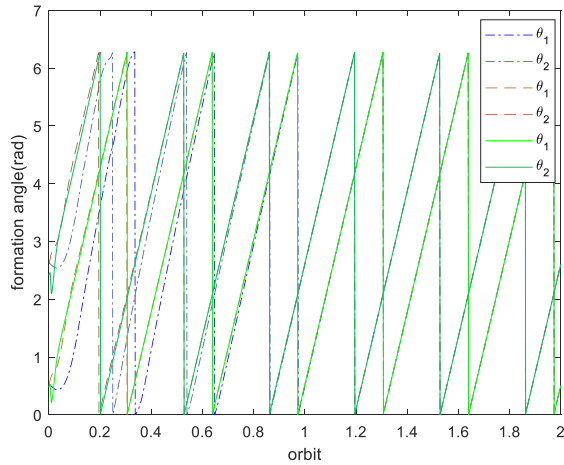Fig. 6.   Nondimensional length of the tethers.

Fig. 7.   Formation angles.

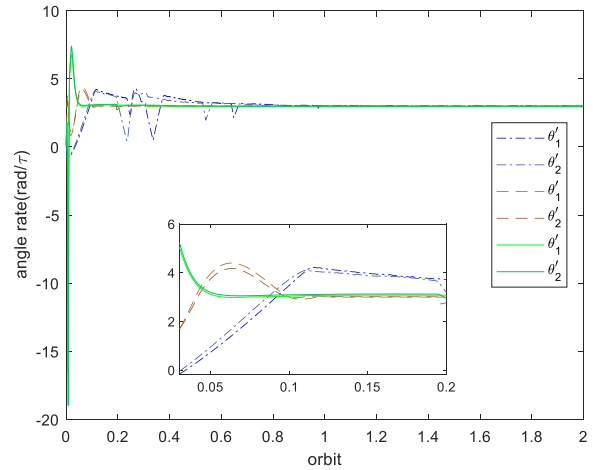
Fig. 8.   Rate of the formation angle.

TABLE II
COMPARISON OF THE CONVERGENCE (CASE OF TETHER IN FIG. 6)

	Scheme 1	Scheme 2	Scheme 3
Convergence time from initial condition to sliding surface	chattering around the manifold	0.063 orbits	0.028 orbits
Convergence time on sliding manifold	chattering around the manifold	0.9461 orbits	0.4096 orbits
Total time from initial condition to final stabilization	1.04 orbits	1.01 orbits	0.44 orbits

improved STSMC scheme are used for the simulation comparison. All the simulation results are shown in Figs. 6–13, which will be detailed discussed. The representations of each scheme for comparison are given as follows.

Scheme 1: The classic STSMC proposed in [19] and [20] with a linear sliding variable given as $\sigma_i = e_i + ce_i'$.

Scheme 2: An improved STSMC given in (21) with a linear sliding variable given as $\sigma_i = e_i + ce_i'$.

Scheme 3: The proposed scheme given in (18) and (21), namely, an improved STSMC with a nonlinear sliding variable.

Nondimensional lengths of the tethers in triangle formation are plotted in Fig. 6. The green full lines represent the results acquired by the proposed scheme (called scheme 3), while the blue dash-dot lines and brown dash lines denote scheme 1 and scheme 2, respectively. Clearly, all the schemes perform well. With the proposed scheme, the state convergence is more quick and stable, and the exact convergence time is compared and given in Table II. From the table, it is obvious that the sliding variable under the proposed scheme can achieve the sliding manifold more quickly compared to schemes 1 and 2. When the sliding manifold is reached, the traditional linear sliding variable is reduced to $\varepsilon_{i1}' = -c\varepsilon_{i1}$. The convergence on the sliding manifold is exponent reaching $\varepsilon_{i1}(t) = \varepsilon_{i1}(0)e^{-c\tau}$,

specifically an asymptotic stable. For the proposed nonsingular sliding variable (15), the sliding dynamics on the manifold ($\varepsilon_{i1} \to 0$) $\varepsilon_{i2}' = -\kappa_2|\varepsilon_{i2}|^{\lambda_2-1}\varepsilon_{i2}$ is finite convergence, which has been discussed in Remark 7. It notes that trajectories of the tethers are almost completely overlapped. This high consistency is the first requirement to maintain the formation of the tethered triangle system. If the convergence of each tether is not uniform, the formation cannot be stably deployed.

Similarly, for the formation angle θ_1 and θ_2 in Fig. 7, the convergence under the proposed scheme is quicker than the others. There are two notable points of the formation angles. First, control gains of each dynamics equation should be the same, and the angles of the formation can keep in a stable value. Second, due to the expression $\theta_i = \theta_i \pm 2k\pi$ ($i \in \mathbb{N}^+$), the trajectories of θ_1 and θ_2 are plotted in the range $[-2\pi, 2\pi]$.

According to the dynamic analysis in Section III, it is known that the angular rate of each tether is important to the formation keeping. First, the angular rate should satisfy the condition (12); second, the angle rate of each tether should try to be consistent during the formation deployment and maintaining; third, to fulfill condition (12), the angular rate of the formation should be achieved as quickly as possible. Fig. 8 shows the angular rate θ_1' and θ_2' with different schemes. It is obvious that the proposed control scheme performs better results, specifically the rapidity and consistency.

The sliding variables σ_{Λ_i} and σ_{θ_i} under the scheme (15) are plotted in Figs. 9 and 10, respectively. The sliding variable of nondimensional tether under the proposed scheme can converge to 0 within 0.05 NT, and the formation angle is within 0.1 NT. Similar to the conclusions of Figs. 6 and 7, compared
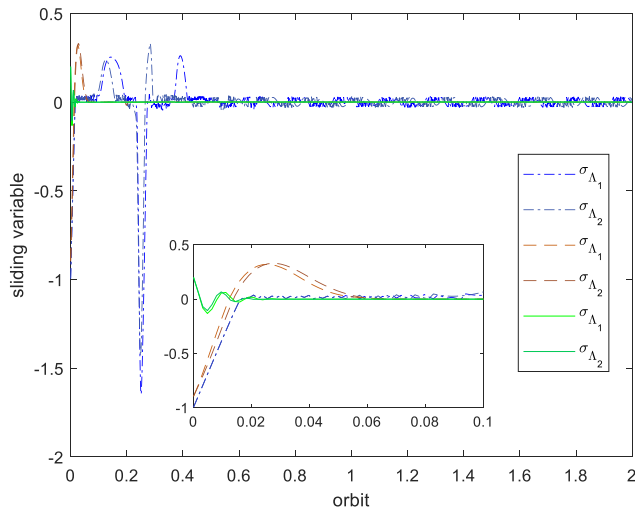
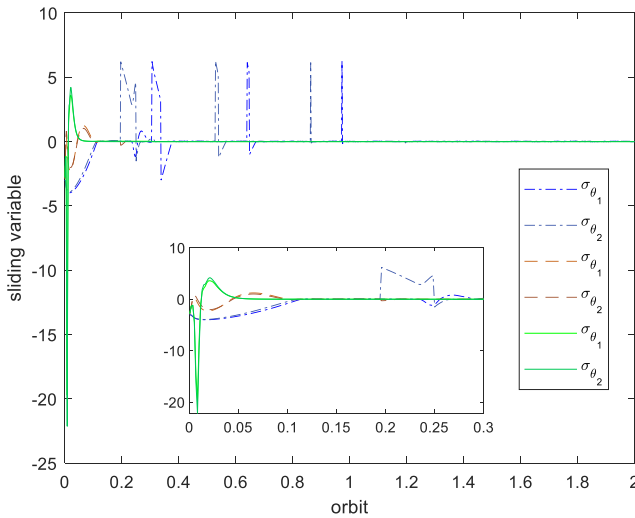Fig. 9. Sliding variables of nondimensional tether.

Fig. 10. Sliding variables of the formation angle.
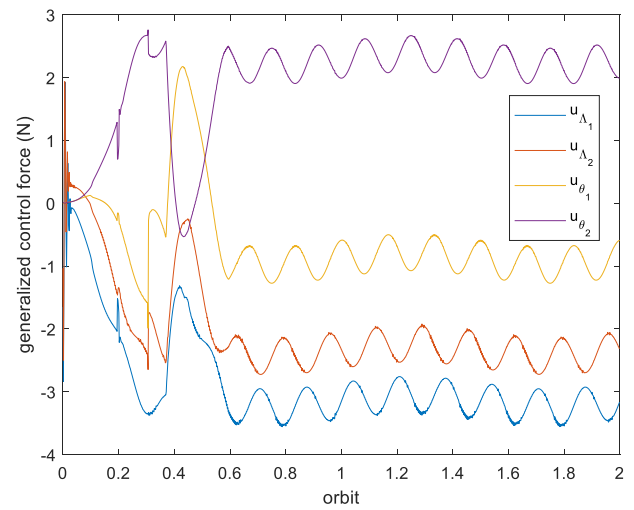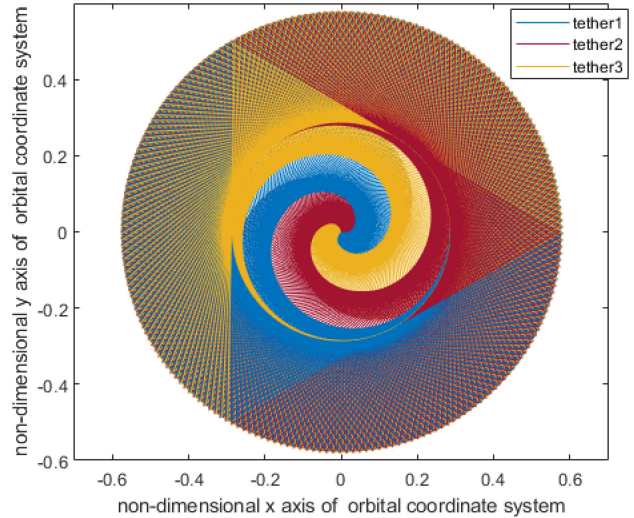

Fig. 11. Generalized control forces.

Fig. 12. Tethered triangle formation in full print version.
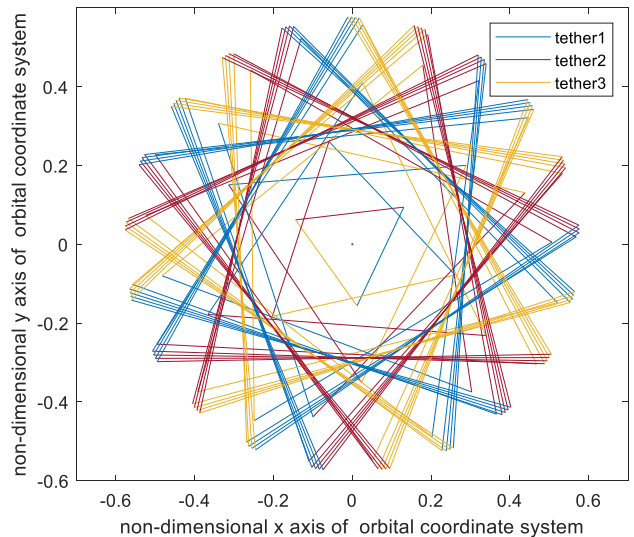
Fig. 13. Tethered triangle formation in simple version.

to schemes 1 and 2, the sliding variables can converge to sliding manifold more quickly under the proposed scheme. Besides, from the comparison of Fig. 9 and Fig. 10, it is shown that the sliding variables of the nondimensional tether perform better than the formation angle. It stems from the fact that the desired tether length is a constant, while the formation angle should track a dynamic trajectory. The generalized control force of each state is given in Fig. 11. Clearly, the traditional chattering problem of sliding-mode control has been improved.

Finally, the integral formation of the tethered triangle system during the deployment has been plotted in Figs. 12 and 13, where Fig. 12 is a full print version, and Fig. 13 is a simple version. In Fig. 12, the process of the deployment can be completely presented, in which blue, red, and yellow represent three tethers in the triangle tethered formation. As explained earlier, a symmetrical formation is very important to the deployment; while asymmetry may lead to tether's slack. Tether's slack in space is very dangerous because it is uncontrollable and twisting. It seems that the formation is kept well during the entire deployment. To check the exact formation, a simple version (every 30 plots) of Fig. 12 is given in Fig. 13.

It is shown that when the system is deployed to the desired formation of a stable condition, the spinning period is about 2.1 NT. Because the result of the centroid trajectory of the

triangle divided by the angular velocity is not an integer, the triangle cannot be completely overlapping. It can be seen that the formation is controlled perfectly during the entire process, specifically intact, symmetric, and uniformly rotating.

VI. Conclusion

In this article, a triangle tethered formation system for space observation was fully studied, including the dynamics modeling, analysis, and controller design of the spinning deployment. According to the dynamic analysis without any external control force, a natural stable spinning condition was acquired. The numerical simulation proved that the triangle system can keep in a symmetrical formation of the derived condition. The proposed scheme consists of a nonsingular nonlinear sliding variable and a second-order sliding-mode controller, which can guarantee both the speed of convergence and alleviation of the chattering problem. The finite converge time was estimated based on the Lyapunov proof and a detailed discussion of the convergence conditions. The proposed scheme was comprehensively compared with the classic super-twisting sliding-mode controller, and an improved super-twisting sliding-mode controller but without a nonsingular sliding variable. The effects of improved STSMC and the nonsingular sliding variable have been discussed. All the results showed that the states under the proposed scheme can converge more quickly, specifically to the manifold and on the manifold. Besides the single state analysis, the entire formation during the deployment has been given at last. It shows that the formation is kept perfect during the entire process.

In future work, different tethered formation systems will be studied, specifically the stereoscopic configuration, such as a double-pyramids formation. For a stereoscopic configuration, more complex dynamics and strong coupled in-plane and out-of-plane formation angles make the control problem more complicated. All the problems will be studied in further work.

References

[1] M. Cosmo and E. Lorenzini, *Tethers in Space Handbook*, 3rd ed. Cambridge, MA, USA: NASA/Marshall Space Flight Center (MSFC) by Smithsonian Astrophysical Observatory, 1997, pp. 1–35.

[2] A. K. Misra and V. J. Modi, "A survey on the dynamics and control of tethered satellite systems," *Adv. Astronautical Sci.*, vol. 62, pp. 667–719, Sep. 1986.

[3] F. Zhang and P. Huang, "Fuzzy-based adaptive super-twisting sliding-mode control for a maneuverable tethered space net robot," *IEEE Trans. Fuzzy Syst.*, early access, Apr. 6, 2020, doi: 10.1109/TFUZZ.2020.2985325.

[4] V. J. Modi, P. K. Lakshmanan, and A. K. Misra, "Dynamics and control of tethered spacecraft: A brief overview," in *Proc. AIM Dyn. Specialist Conf.*, Long Beach, CA, USA, 1990, pp. 42–57.

[5] M. Kim and D. C. Hall, "Control of a rotating variable-length tethered system," *J. Guid. Control Dyn.*, vol. 27, no. 5, pp. 849–858, Oct. 2004.

[6] K. Nakaya, M. Iai, O. Mori, and S. Matunaga, "On Formation deployment for spinning tethered formation flying and experimental demonstration," in *Proc. 18th Int. Symp. Space Flight Dyn. (ESA SP)*, 2004, p. 531.

[7] K. D. Kumar and T. Yasaka, "Rotating formation flying of three satellites using tethers," *J. Spacecraft Rockets*, vol. 41, no. 6, pp. 973–985, Jun. 2004.

[8] E. Topal and U. Daybelge, "Dynamics of a triangular tethered satellite system on a low earth orbit," in *Proc. 2nd Int. Conf. Recent Adv. Space Technol.*, 2005, pp. 218–222.

[9] P. Williams, "Optimal deployment and offset control for a spinning flexible tethered formation," in *Proc. AIAA Guid. Navig. Control Conf.*, Keystone, CO, USA, Aug. 2006, pp. 1–26.

[10] P. Williams and P. Trivailo, "On the optimal deployment and retrieval of tethered satellites," in *Proc. AIAA/ASME/SAE/ASEE Joint Propulsion Conf. Exhibit*, 2005, pp. 1–31.

[11] D. T. Leisawitz *et al.*, "SPECS: The kilometer-baseline far-IR interferometer in NASA's space science roadmao," in *Proc. Int. Soc. Opt. Photon.*, vol. 5487, 2004, pp. 1527–1538.

[12] S.-J. Chung, E. Kong, and D. Miller, "Dynamics and control of tethered formation flight spacecraft using the SPHERES testbed," in *Proc. AIAA Guid. Navig. Control Conf. Exhibit*, 2005, pp. 1–26.

[13] Z. Guang, L. Yuyang, and B. Liang, "Observer enhanced control for spin-stabilized tethered formation in earth orbit," *Acta Astronautica*, vol. 145, pp. 216–228, Apr. 2018.

[14] G. Zhai, F. Su, J. Zhang, and B. Liang, "Deployment strategies for planar multi-tethered satellite formation," *Aerosp. Sci. Technol.*, vol. 71, pp. 475–484, Dec. 2017.

[15] R. Qi and A. Misra, "Dynamics of double-pyramid satellite formations interconnected by tethers and coulomb forces," *J. Guid. Control Dyn.*, vol. 39, no. 6, pp. 1265–1277, 2016.

[16] Z. Zhang, H. Yang, B. Jiang, V. Cocquempot, and Y. Cheng, "Decentralised fault-tolerant control of tethered spacecraft formation: An interconnected system approach," *IET Control Theory A*, vol. 11, no. 17, pp. 3045–3055, 2017.

[17] J. Qin, G. Zhang, W. X. Zheng, and Y. Kang, "Adaptive sliding mode consensus tracking for second-order nonlinear multiagent systems with actuator faults," *IEEE Trans. Cybern.*, vol. 49, no. 5, pp. 1605–1615, May 2019.

[18] D. Yao, H. Li, R. Lu, and Y. Shi, "Distributed sliding-mode tracking control of second-order nonlinear multiagent systems: An event-triggered approach," *IEEE Trans. Cybern.*, vol. 50, no. 9, pp. 3892–3902, Sep. 2020, doi: 10.1109/TCYB.2019.2963087.

[19] M. Zhihong and X. H. Yu, "Terminal sliding mode control design of MIMO linear systems," *IEEE Trans. Circuits Syst. I, Fundam. Theory Appl.*, vol. 44, no. 11, pp. 1065–1070, Nov. 1997.

[20] A. Levant, "Robust exact differentiation via sliding mode technique," *Automatica*, vol. 34, no. 3, pp. 379–384, 1998.

[21] Y. B. Shtessel, J. A. Moreno, F. Plestan, L. M. Fridman, and A. S. Poznyak, "Super-twisting adaptive sliding mode control: A Lyapunov design," in *Proc. 18th IEEE Conf. Decis. Control*, Atlanta, GA, USA, 2010, pp. 5109–5113,

[22] J. A. Moreno and M. Osorio, "Strict Lyapunov functions for the super-twisting algorithm," *IEEE Trans. Autom. Control*, vol. 57, no. 4, pp. 1035–1040, Apr. 2012.

[23] R. Seeber, M. Reichhartinger, and M. Horn, "A Lyapunov function for an extended super-twisiting algorithm," *IEEE Trans. Autom. Control*, vol. 63, no. 10, pp. 3426–3433, Oct. 2018.

[24] I. Castillo, L. Fridman, and J. A. Moreno, "Super-twisting algorithm in presence of time and state dependent perturbations," *Int. J. Control*, vol. 91, no. 11, pp. 2535–2548, Nov. 2018.

[25] H. Haimovich and H. De Battista, "Disturbance-tailored super-twisting algorithms: Properties and design framework," *Automatica*, vol. 101, pp. 318–329, Mar. 2019.

[26] Y. Feng, X. Yu, and Z. Man, "Non-singular terminal sliding mode control of rigid manipulators," *Automatica*, vol. 38, no. 12, pp. 2159–2167, 2002.

[27] M. L. Corradini and A. Cristofaro, "Nonsingular terminal sliding-mode control of nonlinear planar system with global fixed-time stability guarantees," *Automatica*, vol. 95, pp. 561–565, Sep. 2018.

[28] F. Zhang and P. Huang, "A novel underactuated control scheme for deployment/retrieval of space tethered system," *Nonlinear Dyn.*, vol. 95, no. 5, pp. 3465–3476, Mar. 2019.

[29] Y. Shtessel, C. Edwards, L. Fridman, and A. Levant, *Sliding Mode Control and Observation*. New York, NY, USA: Springer, 2014.

Fan Zhang (Member, IEEE) received the B.S. degree in detection, guidance and control technology, and the M.S. and Ph.D. degrees in navigation, guidance and control from the School of Astronautics, Northwestern Polytechnical University, Xi'an, China, in 2009, 2012, and 2017, respectively.

She is currently an Associate Research Professor with School of Astronautics, Northwestern Polytechnical University. Her research focuses on the dynamic and control of tethered robotics, intelligent control, and constrained multiagent systems.

He Zhou received the B.D. degree in aerospace engineering from the School of Astronautics, Northwestern Polytechnical University, Xi'an, China, in 2017, where she is currently pursuing the postgraduate degree with the School of Astronautics.

Her research focuses on the dynamics and deployment control of multitethered system.

Panfeng Huang (Senior Member, IEEE) received the B.S. and M.S. degrees from Northwestern Polytechnical University, Xi'an, China, in 1998 and 2001, respectively, and the Ph.D. degree in automation and robotics from the Chinese University of Hong Kong, Hong Kong, in 2005.

He is currently a Full Professor with the School of Astronautics, the Dean of School of Automation, and the Director of Research Center for Intelligent Robotics, Northwestern Polytechnical University. His research interests include robotics, intelligent control, machine vision, and robot teleoperation.

Jian Guo received the B.Sc. and M.Sc. degrees in engineering from Northwestern Polytechnical University, Xi'an, China, in 1998 and 2001, respectively, and the Ph.D. degree in mechanical engineering from the University of Leeds, Leeds, U.K., in 2010.

He is currently an Associate Professor with the Faculty of Aerospace Engineering, Delft University of Technology (TU Delft), Delft, The Netherlands. He is also a Theme Leader of the TU Delft Space Institute, Delft. His research interests include small satellites, spacecraft guidance navigation and control, distributed space systems, and space robots.